








# Study of the ion mobility in defect-laden $\text{ZrO}_2$ under an electric field using neural network with predictions for Born effective charges

Anh Khoa Augustin Lu <sup>1,2,\*</sup>, Naoki Maekawa <sup>1</sup>, Akane Ikeda <sup>1</sup>, Koji Shimizu <sup>3</sup>,  
Hiroshi Masuda <sup>1</sup>, Hidehiro Yoshida <sup>1</sup> and Satoshi Watanabe <sup>1,†</sup>

<sup>1</sup>Department of Materials Engineering, *The University of Tokyo*, Tokyo 113-8656, Japan

<sup>2</sup>Research Center for Materials Nanoarchitectonics (MANA), *National Institute for Materials Science (NIMS)*, Tsukuba 305-0044, Japan

<sup>3</sup>Materials DX Research Center, *National Institute of Advanced Industrial Science and Technology*, Tsukuba 305-8568, Japan



(Received 18 August 2025; revised 12 March 2026; accepted 4 May 2026; published 2 June 2026)

Unusual mass transport behavior in tetragonal  $\text{ZrO}_2$  ceramics has attracted attention under flash events induced by strong electric fields. However, this observation cannot be attributed solely to Joule heating, suggesting the importance of understanding the ion behaviors associated with defective states under a strong electric field. Previous studies have studied the impact of an external electric field but were typically limited to fixed formal charges for the ions. In this work, to incorporate the response of ions to an electric field, we calculate Born effective charges, and use them in addition to the energy and forces to train neural network potentials. Our molecular dynamics simulations using trained models show that under an applied electric field, the diffusivity of oxygen ions is enhanced in defect-laden  $\text{ZrO}_2$  with a preexisting oxygen vacancy, which could be associated with the observed unusual mass transport behavior. This is a milestone towards the accurate description of defect-laden materials under an applied electric field.

DOI: [10.1103/jcsd-dbl2](https://doi.org/10.1103/jcsd-dbl2)

## I. INTRODUCTION

High-strength structural ceramics are known for their hardness, wear resistance, and chemical stability. However, they are typically brittle and have limited plastic deformability. Among them, tetragonal zirconia ( $\text{ZrO}_2$ ) is one of the most widely used examples, with applications in mechanical tools, medical implants, oxygen sensors, and thermal barrier coatings [1–4].

Metastable phases of zirconia can be maintained at room temperature by adding stabilizers such as calcium, magnesium, cerium, or yttrium [5]. When stabilized with a moderate amount of yttria ( $\text{Y}_2\text{O}_3$ ), yttria-stabilized tetragonal zirconia polycrystal (Y-TZP) is known for its combination of mechanical strength and fracture toughness [6]. Recently, unusually rapid sintering and plastic deformation behaviors of Y-TZP under strong electric fields have attracted attention from researchers [7–11].

Cologna *et al.* reported that when Y-TZP is placed under an electric field, the sintering process can be completed in a few seconds at a low temperature of 850 °C instead of several hours at 1450 °C required for conventional sintering [12]. The rapid sintering is associated with the flash event, where the

electrical conductivity nonlinearly increases, and has been observed in oxide ceramics [8], suggesting the enhancement of oxygen mobility in tetragonal  $\text{ZrO}_2$ . It is known that the flash phenomenon is triggered by thermal runaway because of the combination of Joule heating and an increase in electrical conductivity. However, Raj calculated the temperature increase because of Joule heating in a Y-TZP sample during the flash phenomenon and showed that it was several hundred degrees lower than the temperature required to sinter the sample in a few seconds [7]. Therefore, the rapid mass transport cannot be explained by the effect of Joule heating alone. Raj also implied that the action of the electric field and high temperature can significantly increase the mass transport rate by generating a large number of Frenkel pair defects. Motomura and coworkers observed that instead of brittle fracture, large plastic deformation was obtained in Y-TZP under a flash event [13]. They experimentally demonstrated the nonthermal effect of the flash event in accelerating plastic deformation. Itoh *et al.* detected an excessive concentration of charged oxygen vacancies in 3Y-TZP after flash sintering using photoluminescence spectroscopy [14]. These studies highlight the importance of understanding the ion behaviors in defective states, which can be related to the mass transport behaviors promoted nonthermally under flash events.

Several experimental studies suggested the importance of the response of the system to an external electric field in flash sintering phenomena [12,13]. Xu and coworkers theoretically studied oxygen diffusion in zirconia by performing molecular dynamics simulations with a Coulomb-Buckingham potential [15]. They incorporated the effect of the electric field by adding an electrostatic force  $F = qe$ , where  $q$  denotes the formal charge of each ion [16]. These simulations, based on

\*Contact author: LU.Augustin@nims.go.jp

†Contact author: watanabe@cello.t.u-tokyo.ac.jp

TABLE I. Details of the training data.

Structure type	Materials Project ID	Symmetry group	Defect	Charge	Datapoints
Cubic	1565	$Fm\bar{3}m$	Pristine	0	1978
Cubic	1565	$Fm\bar{3}m$	O vacancy	+2	1942
Tetragonal	2574	$P4_2/nmc$	Pristine	0	1999
Tetragonal	2574	$P4_2/nmc$	O vacancy	+2	2000
Tetragonal	754 403	$I4_1/amd$	O vacancy	+2	597
Monoclinic	2858	$P12_1/c1$	O vacancy	+2	1587
				Total	10 103

empirical potentials, suggested that diffusion is mediated by defect formation and migration. However, the accuracy of such empirical potentials remains uncertain, and the use of a fixed formal-charge model neglects the polarization response.

In recent years, the emergence of high-accuracy neural network potentials (NNPs), pioneered by Behler and Parrinello high-dimensional neural network potentials [17], has deeply modified the landscape of molecular dynamics simulations, enabling near-DFT accuracy calculations for a fraction of the cost. Following this breakthrough, several models have been emerging, such as DeepMD [18], SchNet [19], or NequIP [20], which is the basis for Allegro [21] and SevenNet [22].

While NNPs have enabled an accurate description of interatomic interactions, their prediction accuracy may be insufficient for the cases where the long-range electrostatic interactions play a crucial role. To address this, Zhang *et al.* proposed an extension of DeepMD, DPLR, that adds a deep neural network to predict distributions of spherical Gaussian charges located at ionic and valence-electron Wannier centroids [23]. On the other hand, Shimizu and coworkers developed a neural network architecture, which directly predicts the Born effective charge tensor relevant to a fixed field direction [24] at each time step. Their method does not consider the long-range electrostatic interaction explicitly, in contrast to DPLR. We can expect, however, that their method can describe the ion movements under an applied electric field with sufficient accuracy since the Born effective charge is directly related to the force change owing to an applied electric field.

In this work, we performed first-principles molecular dynamics simulations (FPMD) and density functional perturbation theory (DFPT) of zirconia. As zirconia in its pure form exists with monoclinic symmetry ( $P2_1/c$ ) at room temperature, with a transition to tetragonal symmetry ( $P4_2/nmc$ ) at 1170 °C, then cubic symmetry ( $Fm\bar{3}m$ ) at 2370 °C and a melting point of 2716 °C [1], we included these phases to build a dataset to train neural network potentials with a good accuracy on energy, forces and Born effective charges. Our molecular dynamics simulations confirm previous results that the presence of oxygen vacancies enhances the diffusivity, but more importantly, reveal that the applied electric field further increases it in the direction of the electric field. While the present study focuses on pure  $ZrO_2$ , the insight into oxygen ion mobility under an electric field and in the presence of oxygen vacancies provides qualitative guidance for the more complex yttria-stabilized zirconia.

Our results are an important milestone towards the understanding of the properties of ceramics under an electric

field. More generally, their application to ionic systems should provide valuable insights into their response to an applied electric field.

## II. METHODOLOGY

### A. First-principles calculations

First-principles molecular dynamics (FPMD) calculations were performed to generate atomic configurations to build the training set for training machine learning potentials (MLPs) using the Vienna *Ab initio* Simulation Package (VASP) [25,26]. We used the Perdew-Burke-Ernzerhof (PBE) exchange-correlation functional [27] and the projector-augmented-wave (PAW) method [28] for describing the interaction between inner-shell electrons and nuclei. The energy cutoff for plane waves was set to 520 eV, spin polarization was considered, and we used Monkhorst-Pack  $k$ -point sampling [29]. We used a  $2 \times 2 \times 2$  grid for cubic  $ZrO_2$  ( $Fm\bar{3}m$ ),  $3 \times 3 \times 2$  and  $3 \times 3 \times 1$  for the two tetragonal phases of  $ZrO_2$  ( $P4_2/nmc$  and  $I4_1/amd$ ), and  $2 \times 2 \times 2$  for monoclinic  $ZrO_2$  ( $P12_1/c1$ ). The Materials Project ID [30] for each initial structure is listed in Table I. For molecular dynamics simulations, the time step was set to 1 fs. For each structure, 100-ps simulations at constant volume and temperature (NVT ensemble) were performed. A snapshot was taken every 1 ps. For each snapshot, density functional perturbation theory (DFPT) was used to calculate the Born effective charges [31]. The energy convergence criterion was set to 0.0003 eV for FPMD calculations and  $10^{-6}$  eV for DFPT calculations.

For each structure, temperature values were 1300, 1500, 1700, and 1900 K, and structures with strain values of  $-2\%$ ,  $-1\%$ ,  $0\%$ ,  $1\%$ , and  $2\%$  were built. For structures with an oxygen vacancy, we considered +2 charged vacancies by adding a homogeneous background charge in VASP. In total, the training dataset for the proposed MLPs contained 10 103  $ZrO_2$  snapshots. The details can be found in Table I.

### B. Neural networks

In this work, we develop neural network (NN) potentials in order to describe not only the interatomic interactions, but also the impact of an applied electric field, following the methodology introduced by Shimizu and coworkers [24]. Specifically, a conventional NN of the Behler-Parrinello type [17], hereby denoted by NNP, is dedicated to the calculation of energy and forces without an electric field, and a NN is dedicated to the prediction of Born effective charges for each ion and is denoted by BEC-NN.

In the formalism of NNP, atomic forces can be calculated by applying the chain rule

$$F_j = -\frac{\partial U}{\partial u_j} = -\frac{\partial U}{\partial G_v} \frac{\partial G_v}{\partial u_j}, \quad (1)$$

where  $U$  is the total energy and  $G_v$  are atom-centered symmetry functions (ACSFs) introduced by Behler and Parrinello [17].

The Born effective charge is a tensor that quantifies how the macroscopic polarization in a material changes in response to atomic displacements. It reflects the coupling between atomic motion and an external electric field and is defined by [32].

$$Z_{ij}^* = \Omega \frac{\partial P_i}{\partial u_j} = \frac{\partial F_i}{\partial E_j}, \quad (2)$$

where  $\Omega$  is the cell volume,  $P_i$  is the macroscopic polarization,  $u_j$  are the atomic coordinates,  $F_i$  are the atomic forces, and  $E_i$  is the electric field. It is expressed in units of elementary charge  $e$ . The subscripts  $i$  and  $j$  represent the  $x$ ,  $y$ , and  $z$  directions.

The formalism of NNP was adapted to predict the Born effective charge tensor by first replacing  $U$  by  $-\frac{\Omega}{e}P_i$  and  $F_j$  by  $Z_{ij}^*$  and by preserving directional information in the inputs via vector atomic fingerprints (VAF) [33,34],

$$V_i^{1,\alpha} = \sum_j \frac{R_{ij}^\alpha}{R_{ij}} e^{-\eta(R_{ij}-R_s)} f_c(R_{ij}),$$

$$V_i^{2,\alpha} = 2^{1-\zeta} \sum_j \sum_k (R_{ij} + R_{ik})^\alpha \{1 + \cos(\theta_{ijk} - \theta_s)\}^\zeta$$

$$\times e^{-\eta(\frac{R_{ij}+R_{ik}}{2}-R_s)^2} f_c(R_{ij}) f_c(R_{ik}), \quad (3)$$

where  $\eta$  and  $\zeta$  are width parameters. Importantly,  $R_{ij}$  and  $R_{ik}$  are the atomic vectors of atom  $i$  with atom  $j$  and atom  $k$ , respectively.  $\theta_{ijk}$  is the angle between atoms  $i$ ,  $j$ , and  $k$  at vertex  $i$ .  $\alpha$  represents the direction, either  $x$ ,  $y$ , or  $z$ .  $R_s$  and  $\theta_s$  define the peak positions and  $f_c$  is the cutoff function, defined in

$$f_c(R_{ij}) = \begin{cases} \frac{1}{2} [\cos(\frac{\pi R_{ij}}{R_c}) + 1] & \text{if } R_{ij} \leq R_c \\ 0 & \text{if } R_{ij} > R_c \end{cases}, \quad (4)$$

where  $R_c$  is the cutoff distance. In this work, the cutoff distance is set to 7 Å. Here, we consider the Born effective charge along a specific direction, assuming an electric field along the  $z$  direction, in other words,  $\vec{E} = E_z$ . In this case, the expression of the relevant components is given as

$$Z_{zj}^* = \Omega \frac{\partial P_z}{\partial V_v^z} \frac{\partial V_v^z}{\partial u_j}. \quad (5)$$

Therefore, the present BEC-NN model requires only VAF with  $\alpha = z$  as its input. Assuming that the forces are a linear function of the electric field, the external forces acting on the ions can be expressed as a function of the BEC,

$$\Delta F_j^{\text{BEC-NN}} = Z_{zj}^* E_z. \quad (6)$$

Finally, the total forces are calculated as the sum of the external forces and the values obtained by the BEC-NN,

$$F_j^{\text{Total}} = F_j^{\text{NNP}} + F_j^{\text{BEC-NN}}. \quad (7)$$

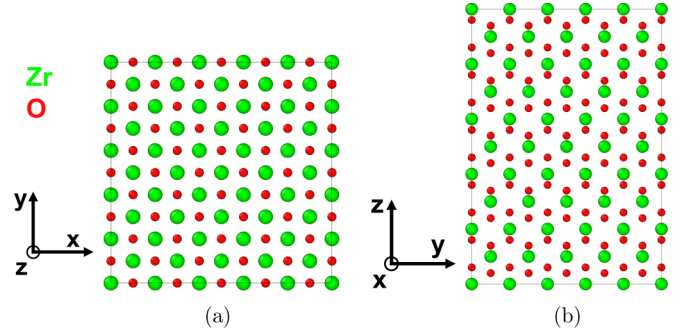


FIG. 1. (a) Top view and (b) side view of the initial structure of pristine ZrO<sub>2</sub> (750 atoms/cell).

This methodology enables accurate simulations of ion dynamics under an electric field.

It is worth noting that in recent years, several groups have developed methods to predict tensor quantities such as the Born effective charge (BEC) tensor using equivariant graph neural networks [35]. Such a method has been developed by Kutana *et al.* to predict the BEC [36]. They adopted the DFPT data obtained in the present work as one of the test cases to demonstrate the validity of their method. Their model has a slightly better accuracy than ours, but at the same time demonstrates the validity of our BEC-NN.

### C. Molecular dynamics simulations under an electric field

Molecular dynamics simulations using the developed neural networks were performed with LAMMPS [37] using the interface developed by Shimizu and coworkers [24]. Calculations were performed in the NPT ensemble using a time step of 1 fs, where the temperature and pressure were controlled using Nosé-Hoover style non-Hamiltonian equations of motion proposed by Shinoda *et al.* [38,39]. For each molecular dynamics simulation, the mean-squared displacements (MSD) were calculated over 1 ns after an initial equilibration period of 100 ps.

We built a  $5 \times 5 \times 5$  supercell of pristine tetragonal ZrO<sub>2</sub> containing 750 atoms, as illustrated in Fig. 1. One oxygen atom was removed to build the supercell with a vacancy, which thus contains 749 atoms.

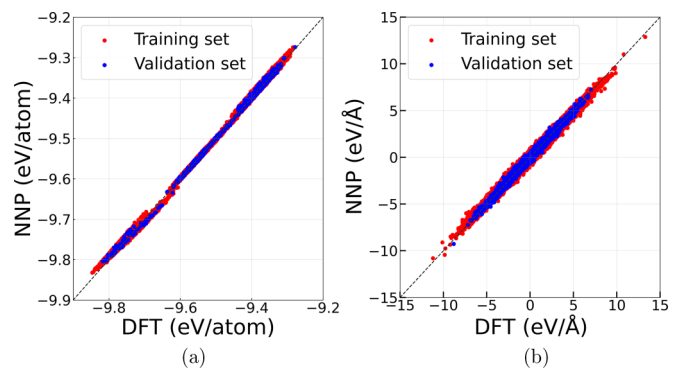
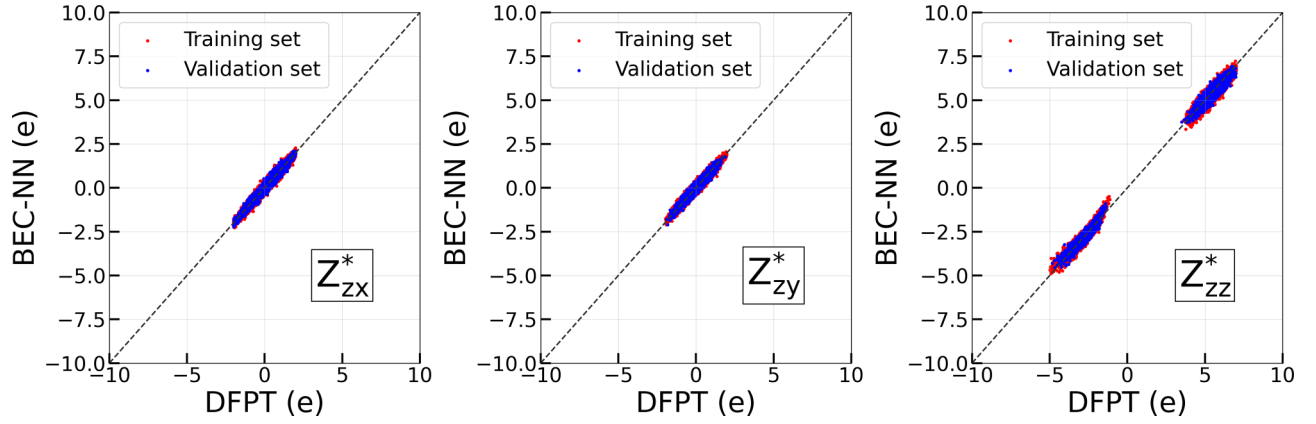


FIG. 2. Comparison between DFT and NNP on (a) the energy and (b) the forces.

FIG. 3. Comparison between DFPT and BEC-NN on the Born effective charges along the  $z$  direction.

The diffusion coefficient is calculated using the expression proposed by Kemp *et al.* [40] for field-dependent ion mobilities, which result from a time-dependent contribution from drift and a contribution from diffusion, as written in below Eq. (8). An example is presented in Fig. S10 within

the Supplemental Material [41]. In the present work, we use Eq. (8) in the direction with a nonzero electric field component ( $z$ ), and below Eq. (9) in other directions,

$$\langle x_i^2 \rangle = (v_{d,it})^2 + 2D_i^*t. \quad (8)$$

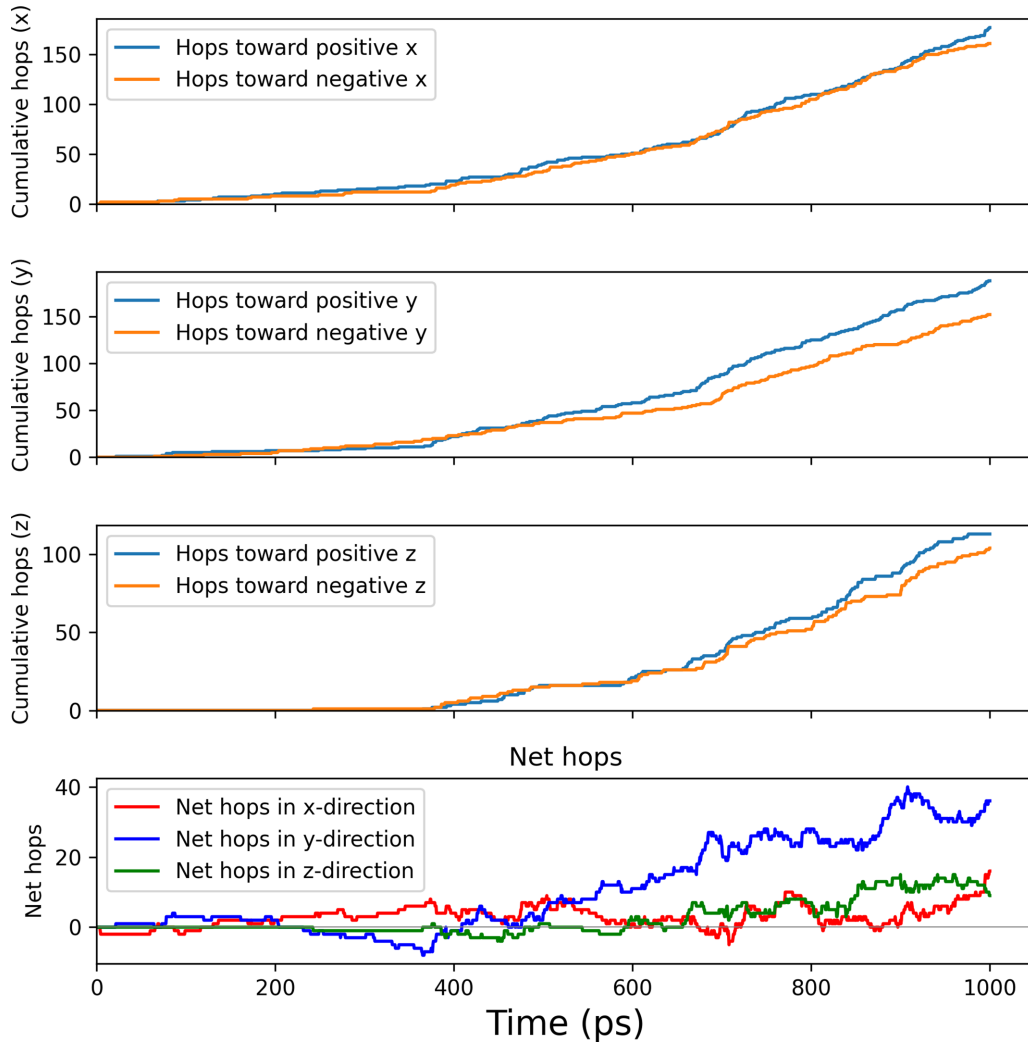


FIG. 4. Hopping events, counted along three directions.

TABLE II. Fitted diffusion coefficient (in  $\text{cm}^2/\text{s}$ ) along (top)  $x$  direction ( $D_x^*$ ) and (bottom)  $z$  direction ( $D_z^*$ ) for oxygen ions. For cases marked by \*, no hopping was observed and the MSD curve had a zero slope.

$D_x^*$	Pristine		With defect	
	No field	0.05 V/Å	No field	0.05 V/Å
T (K)				
1000	0.0*	0.0*	$3.93 \times 10^{-8}$	$2.55 \times 10^{-8}$
1300	0.0*	0.0*	$9.37 \times 10^{-8}$	$7.47 \times 10^{-8}$
1500	$2.43 \times 10^{-7}$	$2.85 \times 10^{-7}$	$1.93 \times 10^{-7}$	$5.36 \times 10^{-6}$
1700	$2.49 \times 10^{-6}$	$4.68 \times 10^{-6}$	$3.93 \times 10^{-6}$	$4.51 \times 10^{-6}$
1900	$5.99 \times 10^{-6}$	$7.72 \times 10^{-6}$	$5.15 \times 10^{-6}$	$1.12 \times 10^{-5}$

$D_z^*$	Pristine		With defect	
	No field	0.05 V/Å	No field	0.05 V/Å
T (K)				
1000	0.0*	0.0*	$1.06 \times 10^{-8}$	$4.15 \times 10^{-8}$
1300	0.0*	0.0*	$3.52 \times 10^{-8}$	$1.61 \times 10^{-7}$
1500	$2.12 \times 10^{-7}$	$1.32 \times 10^{-7}$	$1.15 \times 10^{-7}$	$1.26 \times 10^{-5}$
1700	$2.87 \times 10^{-6}$	$1.52 \times 10^{-5}$	$3.86 \times 10^{-6}$	$1.27 \times 10^{-5}$
1900	$4.69 \times 10^{-6}$	$3.36 \times 10^{-5}$	$4.73 \times 10^{-6}$	$6.01 \times 10^{-5}$

In absence of an electric field in a given direction, the first term vanishes, and the equation reduces to Einstein's relation in one dimension,

$$\langle x_i^2 \rangle = 2D_i^*t. \quad (9)$$

For comparison purpose, we also performed simulations under identical conditions using a Buckingham-Coulomb potential developed by Xu *et al.* [16].

### III. RESULTS

#### A. Development of neural networks

##### 1. Conventional neural network potential (NNP)

The conventional neural network potential was constructed using a network architecture of 66 input nodes, two hidden layers with 10 nodes and one output node for each atomic

species: [66-10-10-1]. The dataset is split with a 90%–10% repartition into a training set and a validation set. The parity plots are presented in Fig. 2. The root-mean-squared error (RMSE) of the energy and the forces were evaluated at 5.4 (5.1) meV/atom and 0.105 (0.099) eV/Å, respectively, for the training (validation) set.

##### 2. Neural network for Born effective charges (BEC-NN)

The neural network for predicting Born effective charges (BEC-NN) was constructed with a similar architecture, but unlike the NNP, the descriptor is VAF. The neural network consists of two hidden layers with 20 nodes and one output node for each atomic species: [94-20-20-1]. The RMSE of the training and validation sets are, respectively, 0.0938 e and 0.0936 e, leading to good accuracy, as shown in Fig. 3. A discussion of the performance of the BEC-NN with respect to the number of input nodes for VAF can be found in Fig. S1 and Table S-I within the Supplemental Material [41]. The diagonal element  $Z_{zz}^*$  shows that the effective charges can strongly differ from the formal charges, i.e., +4 for Zr and −2 for O, highlighting the importance of predicting accurate charges in order to appropriately describe the ion displacements in molecular dynamics simulations. (More details can be found in Fig. S2 within the Supplemental Material [41].) Similar significant fluctuation of the Born effective charges were also seen in the case of  $\text{Li}_3\text{PO}_4$  [24].

#### B. Molecular dynamics simulations

For both pristine  $\text{ZrO}_2$  and defect-laden  $\text{ZrO}_2$ , we performed molecular dynamics simulations at 1000 K, 1300 K, 1500 K, 1700 K, and 1900 K, with an electric field of 0.0 V/Å, 0.05 V/Å, and 0.1 V/Å along the  $z$  direction. Additional calculations with an electric field of 0.01 V/Å and 0.02 V/Å were also performed for structures with defects. The intensity of the electric field used in our simulations is higher than in experimental setups in order to accelerate the dynamics of the system. Experimental observations of flash sintering span timescales on the order of seconds, which are inaccessible to molecular dynamics simulations that typically operate in the

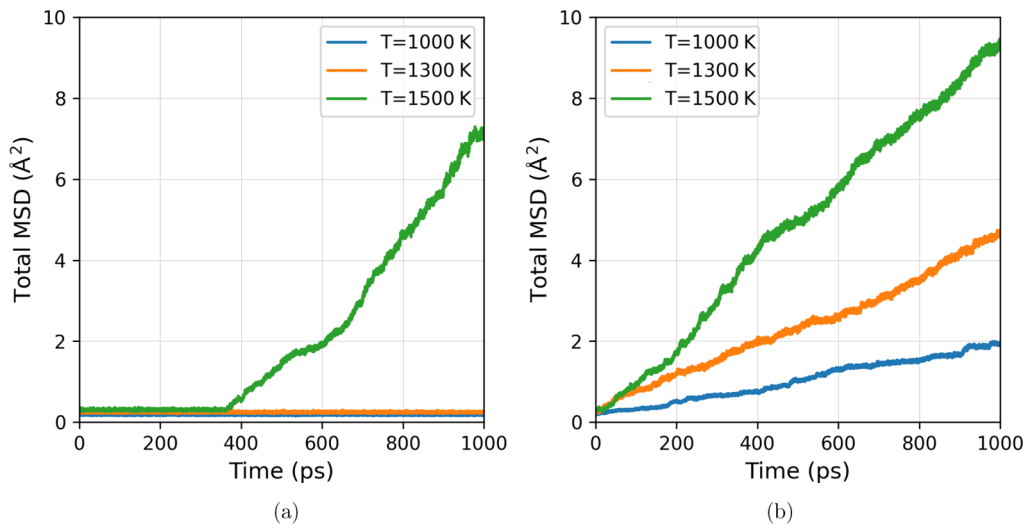


FIG. 5. Comparison between MSD of O atoms in (a) pristine  $\text{ZrO}_2$  and (b) defect-laden  $\text{ZrO}_2$ .



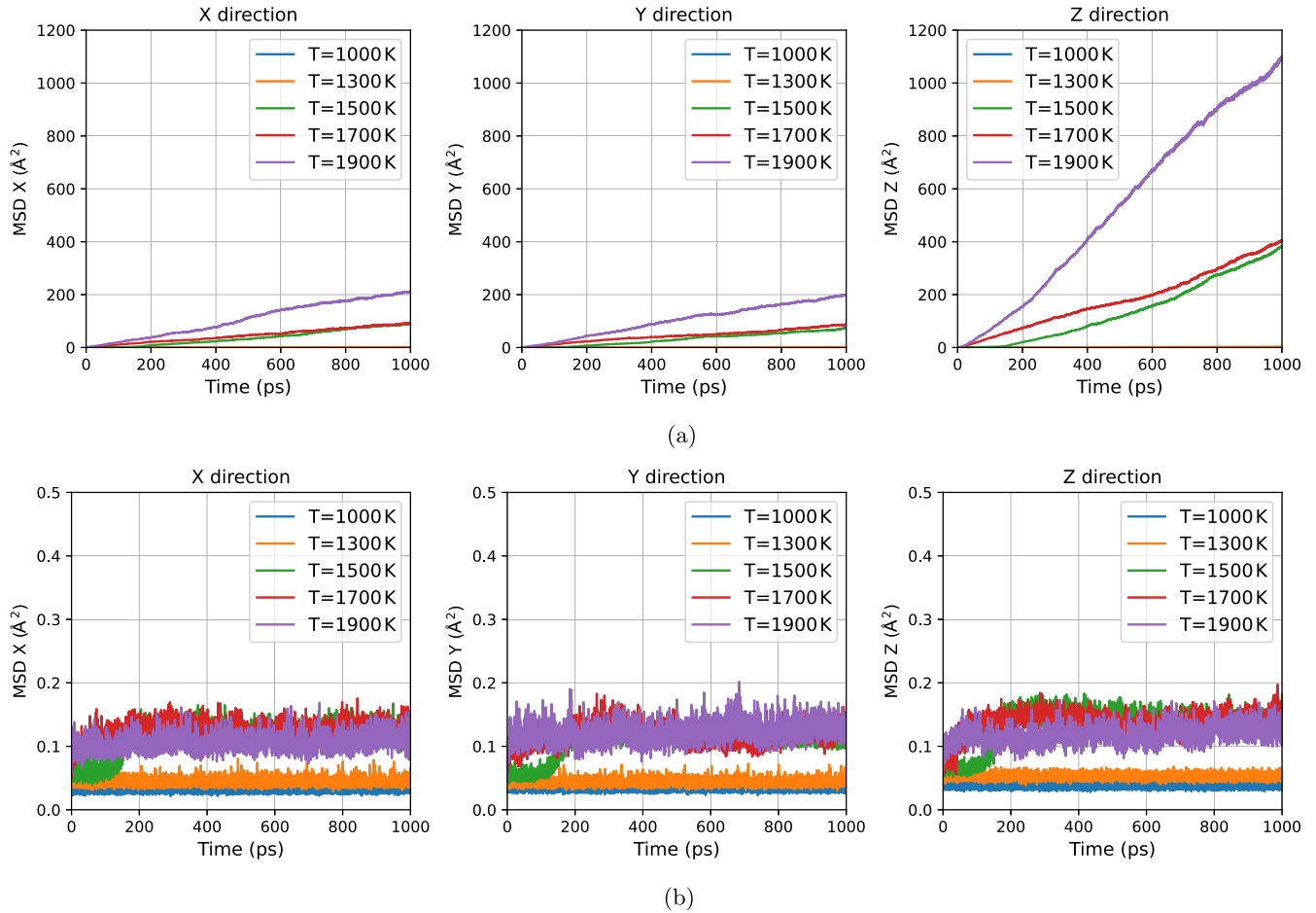


FIG. 6. MSD of defect-laden  $\text{ZrO}_2$  under an electric field of  $0.05 \text{ V/\AA}$ . (a) MSD for O atoms and (b) MSD for Zr atoms.

nanosecond-to-microsecond regime. For each simulation, we first allowed the system to relax for the first 100 ps, then the mean-squared displacement was monitored for 1 ns.

First, we observed that over 1 ns, all structures remained stable except for defect-laden  $\text{ZrO}_2$  at 1900 K and  $0.1 \text{ V/\AA}$ , where void formation was observed. As such, a high electric field is likely destructive, the discussion hereafter will focus on the results with an electric field up to  $0.05 \text{ V/\AA}$ .

### 1. $\text{ZrO}_2$ without electric field

For pristine  $\text{ZrO}_2$  without an electric field, a higher temperature leads to an increase in the mean-squared displacement (MSD) of O atoms, especially at the highest temperatures (1700 K and 1900 K) (see Fig. S3 within the Supplemental Material [41]). In contrast, the MSD profiles of Zr atoms, while slightly increased, reach a plateau. Zr atoms therefore form a rigid framework. The MSD profiles do not depend on the direction (see Fig. S4 within the Supplemental Material [41]). At 1700 K, it was observed that after 136 ps, an O atom moved to an interstitial position ( $\text{O}_i$ ) and created a Frenkel defect. The position of the created vacancy ( $\text{V}_\text{O}$ ) was subsequently taken by a neighboring O atom. Snapshots of this process are shown in Fig. S5 within the Supplemental Material [41]. After the occurrence of this initial defect, hopping from O atoms to the defect position is facilitated, and the MSD

further grows quickly. At 1900 K, this occurred immediately after the simulation started. At 1500 K, the same phenomenon was observed after 364 ps, and is illustrated in Fig. S6 within the Supplemental Material [41]. For this Frenkel defect, we calculated a formation energy of 1.80 eV. Using this value as a minimum theoretical estimate, considering that 1500 K and 1700 K correspond to thermal energies of 0.129 eV and 0.146 eV, respectively, that there are 216 O atoms per atomic cell, and a standard atomic vibration frequency of  $10^{13}/\text{s}$ , we calculated the expected vibration waiting time  $\tau$  to be around 500 ps and 100 ps, respectively, in line with our observed times of 364 ps and 136 ps. Unsurprisingly, this phenomenon was not observed at lower temperatures. To investigate the hopping events more in detail, we monitored atomic displacements every 5 ps and considered that if the displacement along one axis was more than  $1.5 \text{ \AA}$ , then one hopping event has occurred and is accounted for; hopping events towards negative  $x$  (resp.  $y$ ,  $z$ ) and positive  $x$  (resp.  $y$ ,  $z$ ) are counted separately. The net count, obtained by calculating the difference between the number of positive and negative hopping events, represents the global trend. The results, displayed in Fig. 4, show that the number of hopping events slowly increases at first, then accelerates after the first defect is generated. Note that only hopping of O atoms was found. An alternative visual representation of the hopping event count is also shown in Fig. S7a within the Supplemental Material

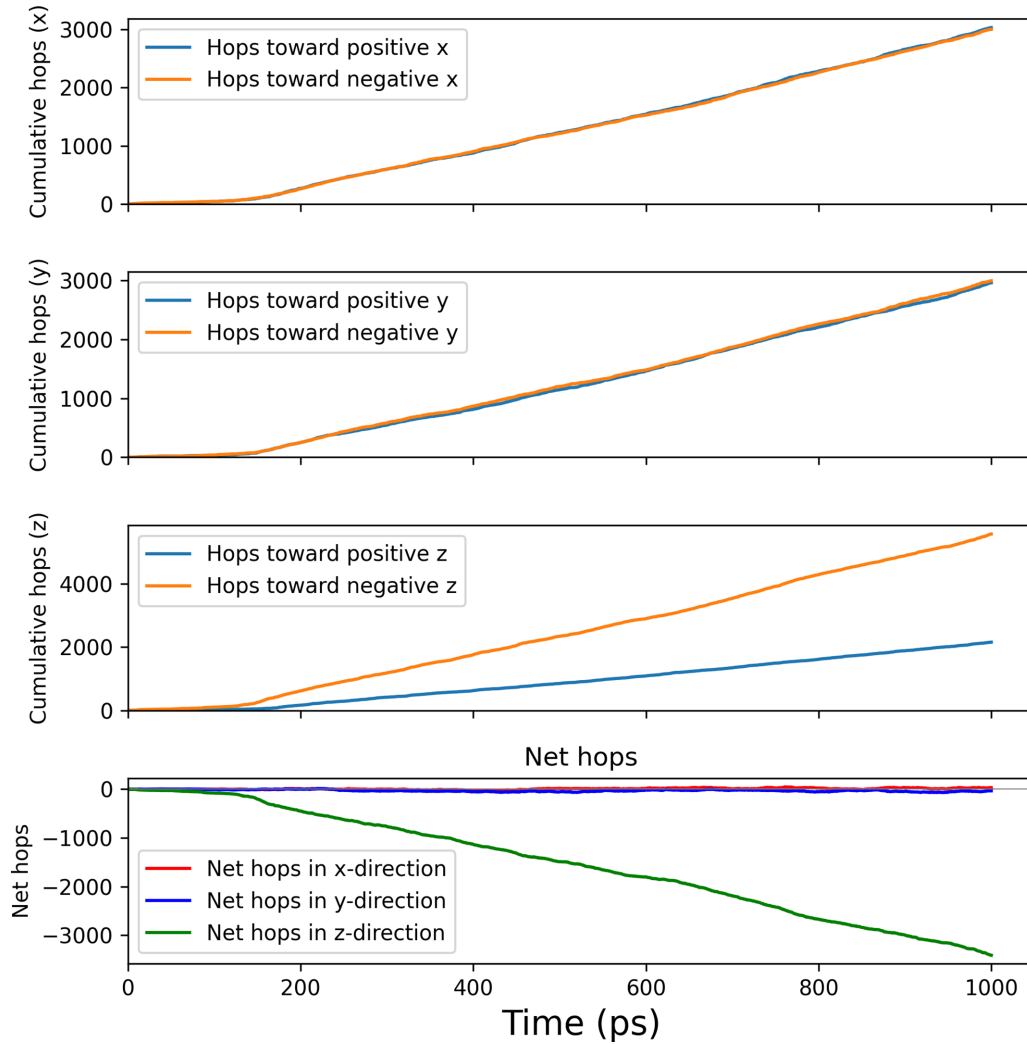


FIG. 7. Hopping events in defect-laden  $\text{ZrO}_2$  at 1500 K under an electric field of  $0.05 \text{ V/\AA}$  along the  $z$  direction.

[41]. In all directions, the number of hopping events towards positive and towards negative values tend to cancel each other, leading to low net hopping counts that mostly hover around the neutral value.

One oxygen atom is removed to create the initial structure, leading to a 749-atom structure. The presence of an oxygen vacancy creates a site for neighboring O atoms to hop into, which enhances diffusion, as shown in Table II. In comparison with pristine  $\text{ZrO}_2$ , hopping is also observed at lower temperatures, as shown in Fig. 5. As expected, the diffusion coefficient is higher for the defect-laden structure compared to pristine  $\text{ZrO}_2$  at low temperature, confirming that preexisting oxygen vacancies promote the diffusion of O atoms.

## 2. Impact of an applied electric field

Next, we investigate the impact of an applied electric field on defect-laden  $\text{ZrO}_2$ . This is possible through the prediction of the Born effective charges with the BEC-NN. We considered an electric field of  $0.05 \text{ V/\AA}$  in the  $z$  direction. As can be seen in the MSD plots shown in Fig. 6, the MSD along the  $z$  direction is greatly increased by the applied electric field, therefore enhancing the diffusion of O ions. It is note-

worthy that using a fixed formal charge model would largely underestimate this phenomenon, as discussed in Figs. S8 and S9 within the Supplemental Material [41].

This is reflected in the hopping event counts as the net hopping along  $z$  drifts towards negative values over time, as shown in Fig. 7. An alternative visualization is provided in Fig. S7b within the Supplemental Material [41]. The diffusion coefficient along the  $z$  direction shows a significant increase under an applied electric field compared to the cases without an electric field, as reported in Table II. This is highlighted by the trajectory lines, as shown in Fig. 8 for the first 400 ps at 1500 K. In pristine  $\text{ZrO}_2$ , only small displacements are visible [Fig. 8(a)]. When an oxygen vacancy is present, displacements increase in all directions compared to the pristine case, as the defect allows hopping to occur [Fig. 8(b)]. Finally, when an electric field is present, the displacements are further increased, with hopping towards negative  $z$  (downward direction) favored, as negatively charged O ions tend to move in the direction opposite the applied electric field [Fig. 8(c)]. At 1500 K and 1700 K, an increase in the diffusion coefficient in defect-laden  $\text{ZrO}_2$  is also observed in directions perpendicular to the applied electric field (Table II). This observation

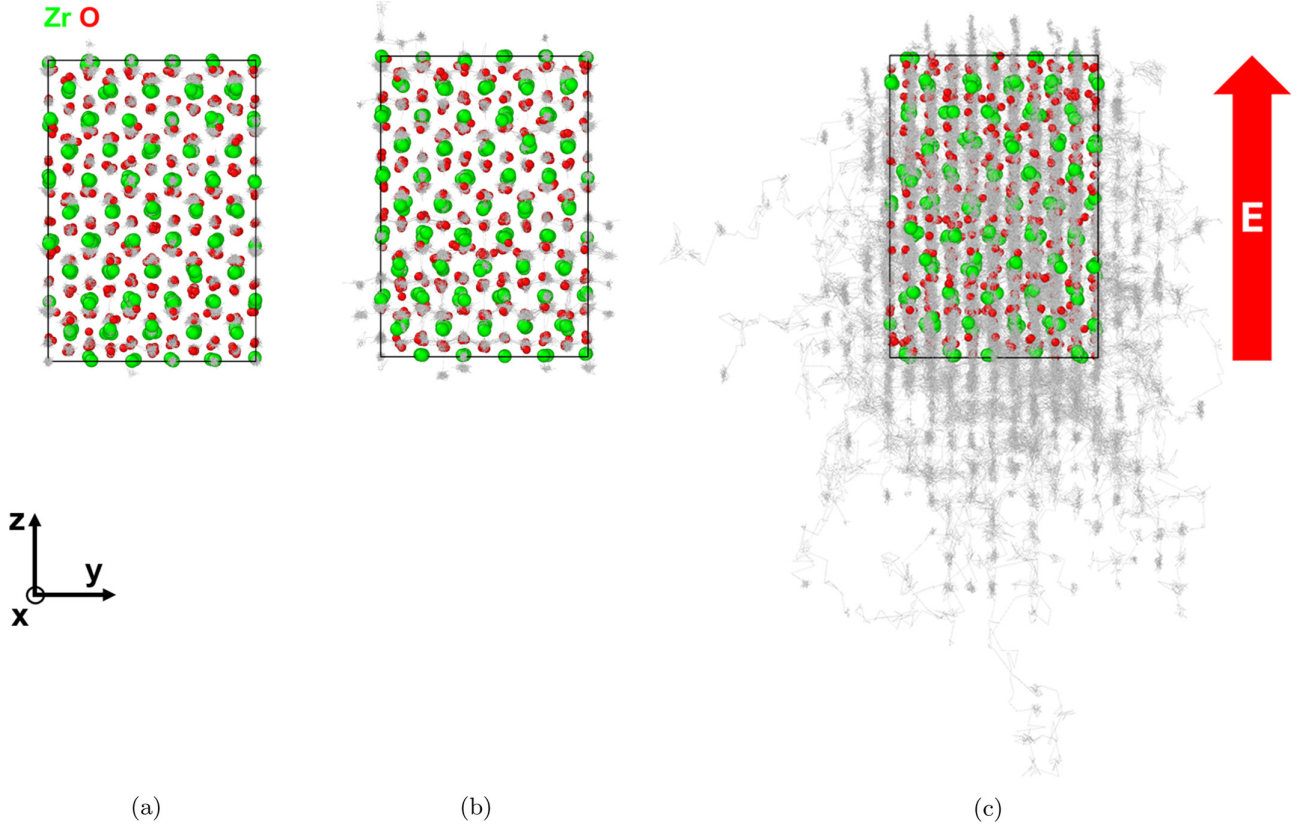


FIG. 8. Trajectory lines (gray lines) over 400 ps for trajectories at 1500 K. Zr (resp. O) atoms are colored in green (resp. red). (a) Pristine, no field, (b) With O vacancy, no field, and (c) With O vacancy, 0.05 V/Å.

may be associated with non-zero nondiagonal elements of the Born effective charge tensor, as can be seen in Fig. 3 for  $Z_{zx}^*$  and  $Z_{zy}^*$ .

The diffusion coefficient  $D^*$ , calculated from the MSD, is shown in Table II. Under no electric field,  $D^*$  is calculated using a linear fit and Einstein's relation. With an electric field along the  $z$  direction, the diffusion coefficient along the  $x$  direction is calculated by linear fit while the diffusion coefficient along the  $z$  direction is calculated using Eq. (8). More details including  $v_d$  can be found in Table S-II within the Supplemental Material [41]. At low temperatures (1000 K), no significant changes are observed with an electric field. At higher temperatures, the diffusion coefficient along the direction of the applied field  $D_z^*$  increases sharply. For instance, in Fig. 9, in defect-laden zirconia at 1500 K and 1700 K, an increase in the diffusion coefficient with respect to the electric field is observed, and this increase is higher in the direction of the electric field  $D_z^*$ .

### C. Nudged elastic band (NEB) calculations

The energy barrier for migration of O atoms from one site to another along the  $z$  direction is evaluated via nudged elastic band calculations, considering a structure with one O vacancy and 14 intermediate structures between the initial and final structures. The energy barrier evaluated by DFT (0.67 eV) was consistent with the value for a +2 charged oxygen defect reported by Eichler (0.61 eV) [42]. The profile given by our neural networks shows a barrier of height 0.58 eV, which is consistent (within 0.1 eV) with DFT results (more details in

Fig. S11 within the Supplemental Material [41]). The BEC predicted by the BEC-NN is consistent with DFPT calculations along the NEB images, showing good transferability (Fig. S12 within the Supplemental Material [41]). The calculated BEC is typically around +5.0 for Zr and -2.7 for O, but can reach +4.5 to 5.4 for Zr and -2.7 to -1.0 for O, which is a significant deviation from the nominal values of +4.0 for Zr and -2.0 for O, and the values vary with the atomic positions of the ions. Therefore, the assumption of constant nominal charges is insufficient for accurately determining the forces arising from an applied electric field. We then calculated the energy barrier for a larger 383-atom cell, which was found to be higher at 0.65 eV. The energy barrier for the small system without electric field is underestimated, likely owing to size effects from the small cell size. As can be seen in Table III, the energy barrier is lowered by the applied electric

TABLE III. Calculated energy barriers for oxygen hopping along the  $z$  direction under varying electric field strengths, using the trained neural network models. Forward and backward barriers correspond to transitions from initial to final and final to initial states, respectively.

Electric field (V/Å)	Forward barrier (eV)	Backward barrier (eV)	Barrier difference (eV)
0.00	0.65	0.65	0.00
0.02	0.59	0.64	-0.05
0.05	0.49	0.62	-0.13



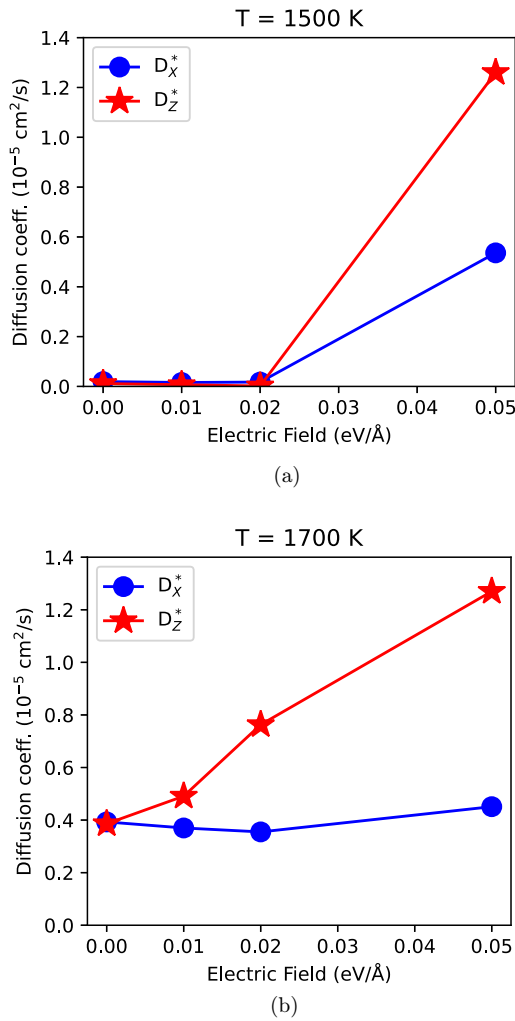


FIG. 9. Evolution of the O ion diffusion coefficient of defect-laden zirconia with respect to the applied electric field at (a) 1500 K and (b) 1700 K.

field, from 0.65 eV without field to 0.59 eV at 0.02 V/Å and 0.49 eV at 0.05 V/Å. We also calculated the energy barrier for two alternative modes oriented at 45° in the  $x$ - $y$  plane, but with a small displacement along  $z$  of  $\pm 0.54$  Å. The barrier without field is around 0.32–0.33 eV, but depending on the  $z$  component of the displacement, can be either reduced to 0.25 eV at 0.05 V/Å (field-assisted) or increased to 0.43 eV at 0.05 V/Å (field-opposed). More details on the energy profiles can be found in Figs. S13 and S14 within the Supplemental Material [41].

#### IV. CONCLUDING REMARKS

In this study, we proposed a neural network potential including prediction of the Born effective charges to study the

ion dynamics in ZrO<sub>2</sub> under an electric field, based on density functional theory and density functional perturbation theory calculations.

Our simulations show that in pristine ZrO<sub>2</sub>, at 1500 K and above, defects appear and drive the dynamics of oxygen ions. The prior presence of an oxygen vacancy allows bypassing the initial time needed to observe defects and increases the diffusion coefficient of oxygen ions.

Under an applied electric field along the  $z$  direction, a net movement of oxygen ions along this direction is observed, which is reflected by the MSD profiles as well as the atomic hopping counts. The diffusion coefficient along this direction is greatly enhanced by the presence of the electric field and could be associated with the unusual mass transport behaviors under flash events. The enhanced oxygen diffusion along  $z$  under an applied field suggests measurable ionic conductivity. While not computed in the present work, our model outputs (energies, forces, and Born effective charges) could be used to obtain Green-Kubo [43,44] or Nernst-Einstein estimates for the conductivity in future work.

Our findings demonstrate the value of a tailored neural network architecture and provide atomistic insight into defect-mediated ion transport in zirconia under an electric field. Such processes are relevant to high-temperature and field-driven phenomena that are known to influence the macroscopic behavior of high-strength ceramics under direct current. Further investigations should explore the role of the stabilizing compounds (such as yttria) as well as other phases of zirconia and their impact on the defect chemistry. Improvements to the neural network architecture, for instance to include all components of the Born effective charge tensor [36], should further improve the accuracy. In the future, more complex systems requiring more configurations in datasets, for instance including explicitly Y, will be studied.

#### ACKNOWLEDGMENTS

This work was supported by the Japan Society for the Promotion of Science (JSPS) Kakenhi Grant No. 24K01284 and the Japan Science and Technology Agency (JST) CREST Grant No. JPMJCR1996. Some of the calculations used in this study were performed using the computer facilities at ISSP Supercomputer Center and Information Technology Center, The University of Tokyo.

#### DATA AVAILABILITY

The data that support the findings of this article are openly available [45], embargo periods may apply.

- [1] J. R. Kelly and I. Denry, State of the art of zirconia for dental applications, *Dent. Mater.* **24**, 289 (2008).
- [2] K. Matsui, H. Yoshida, and Y. Ikuhara, Review: Microstructure-development mechanism during sintering in polycrystalline zirconia, *Int. Mater. Rev.* **63**, 375 (2018).

- [3] H. Masuda, K. Morita, M. Watanabe, T. Hara, H. Yoshida, and T. Ohmura, Ferroelastic and plastic behaviors in pseudo-single crystal micropillars of nontransformable tetragonal zirconia, *Acta Mater.* **203**, 116471 (2021).

- [4] D. Tejero-Martin, M. Bai, J. Mata, and T. Hussain, Evolution of porosity in suspension thermal sprayed YSZ thermal barrier coatings through neutron scattering and image analysis techniques, *J. Eur. Ceram. Soc.* **41**, 6035 (2021).
- [5] J. Chevalier, L. Gremillard, A. V. Virkar, and D. R. Clarke, The tetragonal–monoclinic transformation in zirconia: Lessons learned and future trends, *J. Am. Ceram. Soc.* **92**, 1901 (2009).
- [6] F. Kern and B. Osswald, Mechanical properties of an extremely tough 1.5 mol% yttria-stabilized zirconia material, *Ceramics* **7**, 1066 (2024).
- [7] R. Raj, Joule heating during flash-sintering, *J. Eur. Ceram. Soc.* **32**, 2293 (2012).
- [8] H. Yoshida and T. Yamamoto, Fundamentals and future prospects of flash sintering of advanced ceramics, *J. Jpn. Soc. Powder Powder Metall.* **64**, 523 (2017).
- [9] H. Yoshida and Y. Sasaki, Low temperature and high strain rate superplastic flow in structural ceramics induced by strong electric-field, *Scr. Mater.* **146**, 173 (2018).
- [10] Y. Sasaki, K. Morita, T. Yamamoto, K. Soga, H. Masuda, and H. Yoshida, Electric current dependence of plastic flow behavior with large tensile elongation in tetragonal zirconia polycrystal under a DC field, *Scr. Mater.* **194**, 113659 (2021).
- [11] K. Wang, G. Chen, Q. Wang, X. Fu, and W. Zhou, Unusual electrode-dependent deformation of 3Y-TZP induced by weak electric current in oxygen-lean atmosphere, *Scr. Mater.* **205**, 114220 (2021).
- [12] M. Cologna, B. Rashkova, and R. Raj, Flash sintering of nanograin zirconia in <5 s at 850°C, *J. Am. Ceram. Soc.* **93**, 3556 (2010).
- [13] H. Motomura, D. Tamao, K. Nambu, H. Masuda, and H. Yoshida, Athermal effect of flash event on high-temperature plastic deformation in Y<sub>2</sub>O<sub>3</sub>-stabilized tetragonal ZrO<sub>2</sub> polycrystal, *J. Eur. Ceram. Soc.* **42**, 5045 (2022).
- [14] A. Itoh, T. Tokunaga, A. Kodaira, H. Yoshida, and T. Yamamoto, Variation of photoluminescence intensity depending on the timing of electric field application during isothermal flash sintering for 3 mol%Y<sub>2</sub>O<sub>3</sub>-ZrO<sub>2</sub> polycrystal, *Ceram. Int.* **48**, 28712 (2022).
- [15] R. A. Buckingham, The classical equation of state of gaseous helium, neon and argon, *Proc. R. Soc. Lond. Ser. A* **168**, 264 (1938).
- [16] W. Xu, A. Maksymenko, S. Hasan, J. J. Meléndez, and E. Olevsky, Effect of external electric field on diffusivity and flash sintering of 8YSZ: A molecular dynamics study, *Acta Mater.* **206**, 116596 (2021).
- [17] J. Behler and M. Parrinello, Generalized neural-network representation of high-dimensional potential-energy surfaces, *Phys. Rev. Lett.* **98**, 146401 (2007).
- [18] L. Zhang, J. Han, H. Wang, R. Car, and E. Weinan, Deep potential molecular dynamics: A scalable model with the accuracy of quantum mechanics, *Phys. Rev. Lett.* **120**, 143001 (2018).
- [19] K. T. Schütt, H. E. Sauceda, P.-J. Kindermans, A. Tkatchenko, K.-R. Müller, SchNet—A deep learning architecture for molecules and materials, *J. Chem. Phys.* **148**, 241722 (2018).
- [20] S. Batzner, A. Musaelian, L. Sun, M. Geiger, J. P. Mailoa, M. Kornbluth, N. Molinari, T. E. Smidt, and B. Kozinsky, E(3)-equivariant graph neural networks for data-efficient and accurate interatomic potentials, *Nat. Commun.* **13**, 2453 (2022).
- [21] A. Musaelian, S. Batzner, A. Johansson, L. Sun, C. J. Owen, M. Kornbluth, and B. Kozinsky, Learning local equivariant representations for large-scale atomistic dynamics, *Nat. Commun.* **14**, 579 (2023).
- [22] Y. Park, J. Kim, S. Hwang, and S. Han, Scalable parallel algorithm for graph neural network interatomic potentials in molecular dynamics simulations, *J. Chem. Theory Comput.* **20**, 4857 (2024).
- [23] L. Zhang, H. Wang, M. C. Muniz, A. Z. Panagiotopoulos, and R. Car, Weinan E., A deep potential model with long-range electrostatic interactions, *J. Chem. Phys.* **156**, 124107 (2022).
- [24] K. Shimizu, R. Otsuka, M. Hara, E. Minamitani, and S. Watanabe, Prediction of Born effective charges using neural network to study ion migration under electric fields: Applications to crystalline and amorphous Li<sub>3</sub>PO<sub>4</sub>, *Sci. Technol. Adv. Mater.: Methods* **3**, 2253135 (2023).
- [25] G. Kresse and J. Hafner, *Ab initio* molecular dynamics for liquid metals, *Phys. Rev. B* **47**, 558 (1993).
- [26] G. Kresse and J. Furthmüller, Efficient iterative schemes for *ab initio* total-energy calculations using a plane-wave basis set, *Phys. Rev. B* **54**, 11169 (1996).
- [27] J. P. Perdew, K. Burke, and M. Ernzerhof, Generalized gradient approximation made simple, *Phys. Rev. Lett.* **77**, 3865 (1996).
- [28] P. E. Blöchl, Projector augmented-wave method, *Phys. Rev. B* **50**, 17953 (1994).
- [29] H. J. Monkhorst and J. D. Pack, Special points for Brillouin-zone integrations, *Phys. Rev. B* **13**, 5188 (1976).
- [30] A. Jain, S. P. Ong, G. Hautier, W. Chen, W. D. Richards, S. Dacek, S. Cholia, D. Gunter, D. Skinner, G. Ceder, K. A. Persson, The Materials Project: A materials genome approach to accelerating materials innovation, *APL Mater.* **1**, 011002 (2013).
- [31] S. Baroni, P. Giannozzi, and A. Testa, Green’s-function approach to linear response in solids, *Phys. Rev. Lett.* **58**, 1861 (1987).
- [32] X. Gonze and C. Lee, Dynamical matrices, Born effective charges, dielectric permittivity tensors, and interatomic force constants from density-functional perturbation theory, *Phys. Rev. B* **55**, 10355 (1997).
- [33] V. Botu and R. Ramprasad, Adaptive machine learning framework to accelerate *ab initio* molecular dynamics, *Int. J. Quantum Chem.* **115**, 1074 (2015).
- [34] W. Li and Y. Ando, Comparison of different machine learning models for the prediction of forces in copper and silicon dioxide, *Phys. Chem. Chem. Phys.* **20**, 30006 (2018).
- [35] S. Falletta, A. Cepellotti, A. Johansson, C. W. Tan, M. L. Descoteaux, A. Musaelian, C. J. Owen, and B. Kozinsky, Unified differentiable learning of electric response, *Nat. Commun.* **16**, 4031 (2025).
- [36] A. Kutana, K. Shimizu, S. Watanabe, and R. Asahi, Representing Born effective charges with equivariant graph convolutional neural networks, *Sci. Rep.* **15**, 16719 (2025).
- [37] S. Plimpton, Fast parallel algorithms for short-range molecular dynamics, *J. Comput. Phys.* **117**, 1 (1995).
- [38] G. J. Martyna, D. J. Tobias, and M. L. Klein, Constant pressure molecular dynamics algorithms, *J. Chem. Phys.* **101**, 4177 (1994).
- [39] W. Shinoda, M. Shiga, and M. Mikami, Rapid estimation of elastic constants by molecular dynamics simulation under constant stress, *Phys. Rev. B* **69**, 134103 (2004).

- [40] D. Kemp, A. Tarancón, and R. A. De Souza, Recipes for superior ionic conductivities in thin-film ceria-based electrolytes, *Phys. Chem. Chem. Phys.* **24**, 12926 (2022).
- [41] See Supplemental Material at <http://link.aps.org/supplemental/10.1103/jcsd-dbl2> for details on the parameters used to fit the BEC-NN, the MSD without electric field, a visual representation of the formation of a Frenkel defect, trajectory lines without electric field, MSD profiles under strong electric field, comparison with a fixed formal charge model, MSD along different directions without electric field, and a table with all fitted diffusion coefficient values.
- [42] A. Eichler, Tetragonal Y-doped zirconia: Structure and ion conductivity, *Phys. Rev. B* **64**, 174103 (2001).
- [43] M. S. Green, Markoff random processes and the statistical mechanics of time-dependent phenomena. II. Irreversible processes in fluids, *J. Chem. Phys.* **22**, 398 (1954).
- [44] R. Kubo, Statistical-mechanical theory of irreversible processes. I, *J. Phys. Soc. Jpn.* **12**, 570 (1957).
- [45] A. K. A. Lu, BEC-NN, URL, <https://github.com/AugustinLu/BEC-NN>.